

# Magnons in multiorbital Hubbard models, from Lieb to kagome

Teng-Fei Ying,<sup>1,2</sup> Hugo U. R. Strand,<sup>3</sup> Benjamin T. Zhou,<sup>2</sup> and Erik G. C. P. van Loon<sup>1,4</sup>

<sup>1</sup>*NanoLund and Division of Mathematical Physics,  
Department of Physics, Lund University, Lund, Sweden*

<sup>2</sup>*Thrust of Advanced Materials, The Hong Kong University of Science and Technology (Guangzhou), Guangzhou 511453, China.*

<sup>3</sup>*School of Science and Technology, Örebro University, SE-701 82 Örebro, Sweden*

<sup>4</sup>*Wallenberg Initiative Materials Science for Sustainability,  
Department of Physics, Lund University, Lund, Sweden*

(Dated: January 13, 2026)

We investigate the magnetic orders and excitations in a half-filled Hubbard model that continuously interpolates between the Lieb and kagome lattices. Using self-consistent Hartree–Fock approximation combined with real-time two-particle response functions from the Bethe–Salpeter equation in the random phase approximation, we map the  $U - t'$  phase diagram of the Lieb-kagome lattices, identifying the typical magnetic states and the corresponding magnetic excitation spectra. In addition to gapless Goldstone magnons, the ferrimagnetic and antiferromagnetic symmetry-broken phases also exhibit gapped Higgs magnon bands, which originate from amplitude fluctuations in the order parameter characterizing spontaneous symmetry breaking.

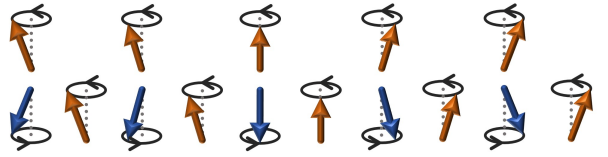
## I. INTRODUCTION

A hallmark of strongly correlated electron systems is the variety of phases that can appear as a result of electron-electron interactions. Out of the simplest single-orbital Hubbard model, exotic metallic, insulating, superconducting, and magnetic phases of matter can emerge [1, 2]. Going beyond a single-orbital Hubbard model, interactions lead to additional phases such as checkerboard charge-density waves [3], exciton condensates [4], and Hund’s metals [5].

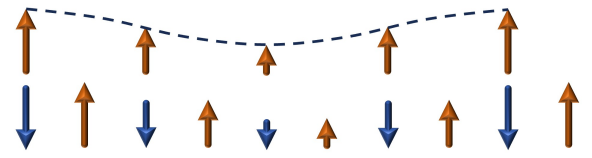
Ordered phases are generally characterized by a (static) order parameter, whereas changes in itinerancy are directly reflected in the single-particle excitation spectrum. On the other hand, the momentum-resolved dynamical susceptibility provides important complementary information, especially in the long-wavelength limit ( $q \rightarrow 0$ ). Notable examples in the charge–orbital sector are the disappearance of low-energy density fluctuations at a gapped–gapless transition [6, 7], as well as the emergence of gapless Goldstone modes in the exciton condensate [4]. More recently, momentum-resolved experiments have reported evidence for Pines’ demon, a neutral, acoustic inter-band collective mode predicted for multi-band systems, in  $\text{Sr}_2\text{RuO}_4$ , which illustrates that multi-orbital materials can host neutral inter-band collective excitations [8].

For magnetic phases and magnetic susceptibilities, which will be the main focus of this work, the basic structure of the susceptibilities [9] in electronic models is similar to purely magnetic (Heisenberg-like) models, although there are effects such as the doping dependence [10, 11] which cannot be directly captured in the Heisenberg model. For a paramagnet with  $SU(2)$  spin symmetry, the dynamic spin susceptibility is rotationally invariant, (i.e.  $\chi^{xx}(\omega, \mathbf{q}) = \chi^{yy}(\omega, \mathbf{q}) = \chi^{zz}(\omega, \mathbf{q})$  and  $\chi^{xy}(\omega, \mathbf{q}) = \chi^{yz}(\omega, \mathbf{q}) = 0$ ), and has a sharp Goldstone mode with a linear dispersion at small  $q$ . In a ferro-

(a) Goldstone (transverse) mode



(b) Higgs (longitudinal) mode



(c) Stoner (single-particle) mode

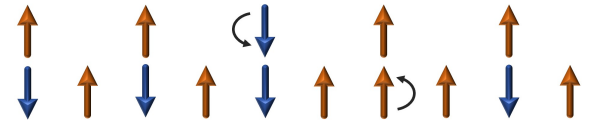


FIG. 1. Illustrations of three types of magnetic excitations in the Lieb lattice: (a) the Goldstone mode, corresponding to a gapless magnon mode; (b) the Higgs mode, representing a gapped (amplitude) magnon from fluctuation of the order parameter; and (c) the Stoner mode (pair), describing single-particle spin-flip excitations.

magnet at  $q = 0$ , there are both Goldstone modes with quadratic dispersion corresponding to the rotation of the order parameter and two types of gapped longitudinal modes, as illustrated in Fig. 1 (a) and (b, c), respectively. In an electronic model of the ferromagnet, the fundamental longitudinal mode is the Stoner excitation of an electron from the majority to the minority band, with an energy given by the exchange splitting. Similarly, the application of an external magnetic field to an intrinsically paramagnetic system of electrons leads to

magnetic excitations with a finite energy given by the Larmor frequency [12]. In multi-band models, the possibility of electronic excitations from occupied minority to empty majority bands makes it possible to have minority magnons [13]. The Goldstone modes in antiferromagnets typically have a linear dispersion in the long wavelength limit, in contrast to the quadratic dispersion of ferromagnets. Additionally, there are gapped flat bands of magnons, i.e., the Higgs mode [14], of the magnetic symmetry-breaking, which has been experimentally observed in the ferromagnetic kagome lattice [15, 16]. Finally, altermagnets have linearly dispersing magnons with a chiral splitting [17–19], in the sense that  $\chi^{+-}(\omega, \mathbf{q})$  and  $\chi^{-+}(\omega, \mathbf{q})$  have different dispersions. Altogether, these observations show that the symmetry and long-wavelength dispersion of magnetic excitations are powerful tools for the characterization of magnetically-ordered electronic phases.

In this work, we study a set of Hubbard models that continuously interpolates between the Lieb and kagome lattice [20], which are found to stabilize a variety of magnetic phases in the Hartree-Fock approximation, including ferrimagnetic and antiferromagnetic phases. We show that the electronic dispersion and, in particular, the magnon spectra of the phases provide powerful tools for understanding the underlying physics. The paper is structured as follows: We first introduce the model and its Hartree-Fock solution (Sec. II A) and discuss the implications of the Lieb and Mermin-Wagner theorem for our results (Sec. II B), followed by the Hartree-Fock phase diagram and order parameters (Secs. III A–III C), the electronic structure (Sec. III D) and finally the magnon spectra (Sec. III E–III B).

## II. MODEL AND METHOD

### A. Hubbard Model: Lieb and kagome

In the context of the Hubbard model, the lattice structure is reflected in the number of orbitals per unit cell and the tight-binding parameters. Mathematically, the tight-binding parameters can be represented as a weighted graph, and it is only the structure of this graph that matters for the model, not its geometrical interpretation. As discussed by Jiang et al. [20], in this way, it is possible to continuously interpolate between the Lieb lattice and the kagome lattice in two dimensions by changing the weights in the graphs, i.e., the hopping parameters.

In both lattices, each unit cell contains three sites. For the Lieb lattice, these are a corner site labeled A and two edge-centered sites labeled B and C, as illustrated in Fig. 2(a). In our model, the hopping between the corner site and an edge-centered site is  $t$ , while the hopping between two edge-centered sites in the same unit cell is  $t'$ . The situation  $t' = 0$  corresponds to the normal Lieb lattice, while  $t' = t$  gives the kagome lattice, shown in Fig. 2(b), so by varying the parameter  $t' \in [0, t]$ , we can

continuously go from Lieb to kagome. The corner site and the edge sites are inequivalent except at  $t' = t$ . We set  $t = 1$  as the unit of energy. Since the lattices in Fig. 2(a–b) are equivalent (weighted) graphs, either one can be used for the implementation. In our implementation, we use the lattice of Fig. 2(a), i.e., a square lattice with three atoms in the unit cell.

For the limit of the Lieb lattice with  $t' = 0$ , the square Bravais lattice with point group  $C_{4v}$  gives the symmetry operations as:

$$E, C_{4z}, \sigma_x, \sigma_y, \sigma_d, \sigma_{\bar{d}}, \quad (1)$$

plus all lattice translations. Here,  $E$  is the identity operator,  $C_{4z}$  is the four-fold rotation symmetry about the  $z$ -axis.  $\sigma_x, \sigma_y, \sigma_d, \sigma_{\bar{d}}$  represent the mirror reflection symmetries about  $x$ -axis,  $y$ -axis, and both diagonal axes, respectively. For a finite  $t'$ ,  $C_{4z}$  is lost, and the lattice has the smaller  $C_{2v}$  point group, with symmetry operations:

$$E, C_{2z}, \sigma_d, \sigma_{\bar{d}}, \quad (2)$$

and the lattice translations. We notice that even for the case of  $t' = 1$  in the model of Fig. 2(a), while reproducing the features of the band structures of the kagome lattice, the lattice geometry will not reach the  $C_{6v}$  point group, in contrast to the standard kagome lattice shown in Fig. 2(b).

In momentum space, the corresponding Brillouin zone is also square, whereas the one corresponding to the triangular lattice would be hexagonal. The square Brillouin zone is shown in Fig 2(c), with high-symmetry points  $\Gamma = (0, 0)$ ,  $X = (\pi, 0)$ ,  $K = (4\pi/3, 2\pi/3)$  and  $M = (\pi, \pi)$ . Note that, in contrast to the square lattice with 1 orbital per cell, here the unit cell with finite  $t'$  itself lacks  $C_{4z}$  rotation symmetry, which is reflected in a reduced symmetry in the Brillouin zone as well. We use the path  $\Gamma$ -X-K-M in the Brillouin zone to visualize the bands. The band structure of the non-interacting model is shown in Fig 2(d) and discussed in App. B, it has a flat band precisely at  $t' = 0$  and  $t' = 1$ , but not anywhere in between [20].

With this definition of the tight-binding model, the Hubbard Hamiltonian is given by

$$\begin{aligned} H = & -t \sum_{\langle i,j \rangle, \sigma} (c_{i\sigma}^\dagger c_{j\sigma} + \text{h.c.}) \\ & -t' \sum_{\langle\langle i,j \rangle\rangle, \sigma} (c_{i\sigma}^\dagger c_{j\sigma} + \text{h.c.}) \\ & +U \sum_i n_{i\uparrow} n_{i\downarrow} - \mu \sum_i (n_{i\uparrow} + n_{i\downarrow}), \end{aligned} \quad (3)$$

where  $c_{i\sigma}^\dagger$  and  $c_{i\sigma}$  are the creation and annihilation operators for an electron with spin  $\sigma$  at lattice site  $i$ , and  $n_{i\sigma} = c_{i\sigma}^\dagger c_{i\sigma}$  is the number operator. The chemical potential  $\mu$  controls the electron density, which is set to half-filling in this study, and  $U$  is the on-site Hubbard interaction.

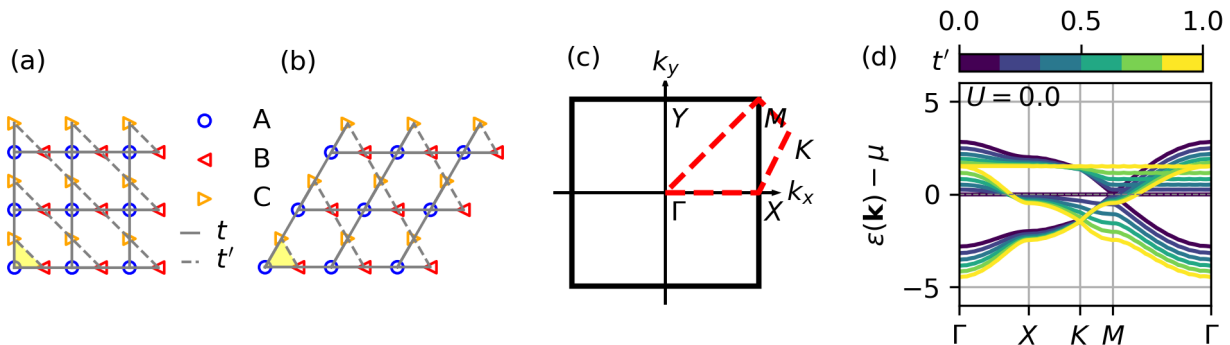


FIG. 2. Schematic of (a) the Lieb and (b) kagome lattices. Sites of sublattices A, B, and C are marked by blue circles, red triangles, and orange triangles, respectively, and the shaded yellow region highlights the three sites (A, B and C) in a single unit cell. Solid and dashed lines refer to the nearest-neighbour (NN) and the next-nearest-neighbour (NNN) hopping amplitude  $t$  and  $t'$ , respectively. By varying  $t'$ , the system is continuously tuned from the ideal Lieb ( $t' = 0$ ) to the ideal kagome ( $t' = t$ ) lattice. (c) The first Brillouin zone and high-symmetry points corresponding to the Lieb lattice. (d) Non-interacting band structures of the Lieb lattice as functions of  $t'$ , plotted along the high-symmetry path in panel (c).

The model is solved at finite temperature using the Hartree-Fock (HF) approximation as implemented in the Toolbox for Research on Interacting Quantum Systems (TRIQS) [21] and its Two-Particle Response Function toolbox (TPRF) [22]. The HF self-consistency loop is seeded with tiny magnetic fields to ensure that symmetry-broken solutions, i.e., the ferromagnetic or ferrimagnetic states, and magnetic frustration of the Lieb-kagome lattice can be found, and that the order parameter of the symmetry-broken solution always has  $\langle S^z \rangle \geq 0$ . We apply these fields in both longitudinal and transverse directions for the symmetry-broken solutions.

To explore the possibility of altermagnetism, we also apply a small staggered field  $S_B^z - S_C^z$ . With this setup, we identify an unconventional altermagnetic state in the half-filled Lieb lattice for certain values of  $U$  and  $t'$ . However, previous studies have shown that this altermagnetic state is stabilized as the true ground state of the Lieb lattice only at fillings  $n = 2$  and  $n = 4$ , rather than at half-filling [23]. Consistent with these findings, we find that at half-filling the altermagnetic state obtained in our calculations is metastable and remains stabilized only in the presence of the external staggered field, rather than constituting a global ground state. Nevertheless, the corresponding band structure and magnetic excitation spectra can still yield insights into altermagnetic behavior in other materials.

In the present study we limit the calculations to solutions with unit-cell translation symmetry, in the sense that the Hartree-Fock single-particle density matrix  $\rho_{i\sigma, j\sigma'} \equiv \langle c_{i\sigma}^\dagger c_{j\sigma'} \rangle$ , where  $i, j \in \{A, B, C\}$  and  $\sigma, \sigma' = \uparrow, \downarrow$ , is the same in every unit cell. From the single-particle density matrix, we extract the site-dependent occupation numbers  $\langle n_{i\sigma} \rangle$  as well as an effective, spin-dependent band structure for the interacting model.

The lattice susceptibility  $\chi(\omega, \mathbf{q})$  is subsequently calculated from the HF solution, also using TPRF. Starting

from the (lesser and greater) single-particle Green's function in real time and momentum space,

$$G^<(t, \mathbf{k}) = i\rho e^{-i\epsilon_{\mathbf{k}}^{\text{HF}} t}, \quad (4)$$

$$G^>(t, \mathbf{k}) = i(\rho - 1)e^{-i\epsilon_{\mathbf{k}}^{\text{HF}} t}, \quad (5)$$

where  $\epsilon_{\mathbf{k}}^{\text{HF}}$  is the Hartree-Fock dispersion, and using the spatial Fourier transform  $G^{\lessgtr}(t, \mathbf{r}) = \mathcal{F}_{\mathbf{k} \rightarrow \mathbf{r}} G^{\lessgtr}(t, \mathbf{k})$ , the bare lattice susceptibility  $\chi_0$  is calculated as the direct product

$$\chi_0(t, \mathbf{r}) = iG^<(t, \mathbf{r})G^>(-t, -\mathbf{r}) - iG^>(t, \mathbf{r})G^<(-t, -\mathbf{r}), \quad (6)$$

and subsequently Fourier transformed back to real frequency and momentum

$$\chi_0(\omega, \mathbf{q}) = \mathcal{F}_{\{t, \mathbf{r}\} \rightarrow \{\omega, \mathbf{q}\}} \{ \chi_0(t, \mathbf{r}) \}. \quad (7)$$

This approach makes it possible to study the real-frequency dependence on dense momentum grids, without having to resort to analytical continuation. This is essential for simultaneously resolving sharp and broad features in the susceptibility, at low and high energy. Finally, the RPA lattice susceptibility is evaluated using the Bethe-Salpeter equation,

$$\begin{aligned} \chi^{\text{RPA}} &= \chi_0 + \chi_0 U \chi^{\text{RPA}} \\ &= \frac{\chi_0}{1 - \chi_0 U}, \end{aligned} \quad (8)$$

which is diagonal in frequency and momentum. The bare ( $\chi_0$ ) and RPA ( $\chi^{\text{RPA}}$ ) susceptibility and the interaction ( $U$ ) are all four-dimensional tensors in the spin-orbital indices.

We will focus on the imaginary part of the dynamical transverse susceptibility,  $\Im \chi^{+-}(\omega, \mathbf{q})$ , which corresponds to the magnetic excitation spectrum, characterizing the dissipative response of the system [13].

## B. Two theorems: Mermin-Wagner and Lieb

Lieb's theorem [24] states that the ground state of an unbalanced, bipartite lattice has a finite total magnetization. Here, bipartite means that the system can be divided into two groups of sublattice sites and that hopping only happens between sites from different groups, and the word "unbalanced" refers to the difference in the number of sites contained in each group. In our model, the lattice is only bipartite at  $t' = 0$  (and unbalanced), so Lieb's theorem holds only there. We note that Lieb's theorem applies to the zero temperature ground state, while our study takes place at finite temperatures.

The Mermin-Wagner theorem states that there is no spontaneous symmetry breaking of continuous symmetries in two-dimensional systems at  $T > 0$  [25]. This theorem rules out ferrimagnetism as the exact solution. However, approximate solutions such as HF and even dynamical mean-field theory are known to show ordered solutions at low temperature, in violation of the Mermin-Wagner theorem. Our interest here is in the physics of magnetic excitations in ferrimagnets, which can be studied with this model and method, even though the exact solution of the model is not ferrimagnetic. In reality, Mermin-Wagner is enforced by very long-wavelength magnetic fluctuations, so that the local physics is often reasonably similar to what is found in approximate, Mermin-Wagner-violating methods [26–28]. We further note that our results obtained through these methods do apply to real 2D materials studied in labs which would always have a finite system size.

## III. RESULTS

### A. Phase Diagram

We present the phase diagram of the Lieb-Kagome lattice in the Hubbard model at half-filling in Fig. 3, in terms of the magnetization  $\langle S^z \rangle$  as a function of Hubbard interaction  $U$  and the hopping parameter  $t'$  at the inverse temperature  $\beta = 10$ , computed by the HF approximation. From Fig. 3, we can (for any fixed  $t'/t$ ) identify the critical interaction  $U_P$  that separates the non-magnetically-ordered (paramagnetic) phase and the magnetically ordered phases. The transition is first order; the magnetization drops to zero as  $U < U_P$ . In addition, the transition from finite average magnetization (the ferrimagnetic phase) to phases with vanishing average magnetization occurs continuously with increasing  $t'$ . The result at lower temperature,  $\beta = 50$  (shown in Fig. 20 in Appendix), has a slightly smaller  $U_P$ .

In the Lieb lattice limit ( $t' = 0$ ),  $U_P$  is found to be relatively small but not zero, as we are at finite temperature. In the HF approximation, this behavior originates from the presence of a flat band at the Fermi energy in the Lieb lattice, where even a small repulsive interaction  $U$  can induce a ferrimagnetic ground state at half-filling.

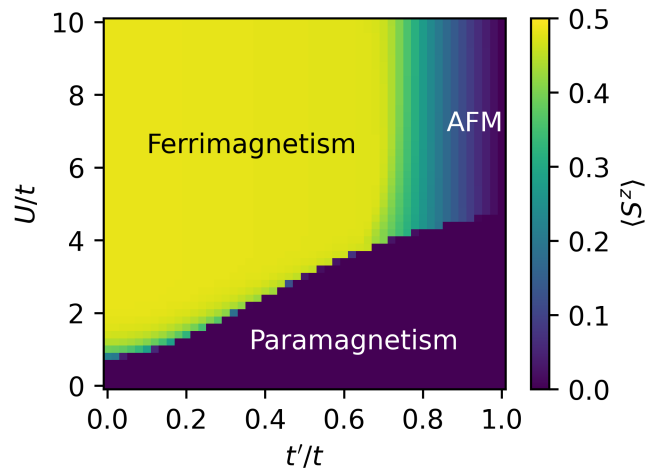


FIG. 3. Phase diagram in the HF approximation of the Lieb-kagome lattice at the inverse temperature  $\beta = 10$ . The heatmap presents the magnetization as a function of  $U$  and  $t'$ . There is a first-order phase transition from the paramagnetic state to a magnetically ordered state, either ferrimagnetic or antiferromagnetic (AFM), with increasing interaction strength, and a continuous transition between the ferrimagnetic and antiferromagnetic state as a function of  $t'$ .

Indeed, the Stoner criterion  $UD(E_F) \leq 1$  implies a vanishing critical  $U$  at  $T = 0$  due to the divergent density of states, which becomes finite when finite temperature is considered.

As  $t'$  increases, the flat band acquires dispersion, and the density of states at the Fermi level is gradually reduced. Consequently, both the local-moment threshold and the ordering threshold shift to larger  $U$ , increasing steadily with  $t'$  up to  $t'/t \sim 0.8$ .

Going towards the kagome lattice ( $t'/t \rightarrow 1$ ), magnetic frustration becomes important, and an antiferromagnetic state on the corner-sharing triangles is found. This antiferromagnetic state only occurs for a narrow range of  $t'$  close to the kagome limit. However, it is important to note that the HF approximation employed here neglects correlation effects beyond the mean field and generally overestimates the stability of symmetry-broken states. As a result, it cannot fully capture the frustration in the kagome lattice accurately. Therefore, the critical  $t'$  at a certain  $U$  for the transition of antiferromagnetic order is larger than that reported in other studies using more sophisticated methods [29, 30].

In addition to the phases shown in the phase diagram of Fig. 3, it is also possible to stabilize solutions with other symmetries, which correspond to local but not global minima in the free energy. An example is an altermagnetic state which can be found by starting the Hartree-Fock self-consistency loop with a small staggered magnetic field.

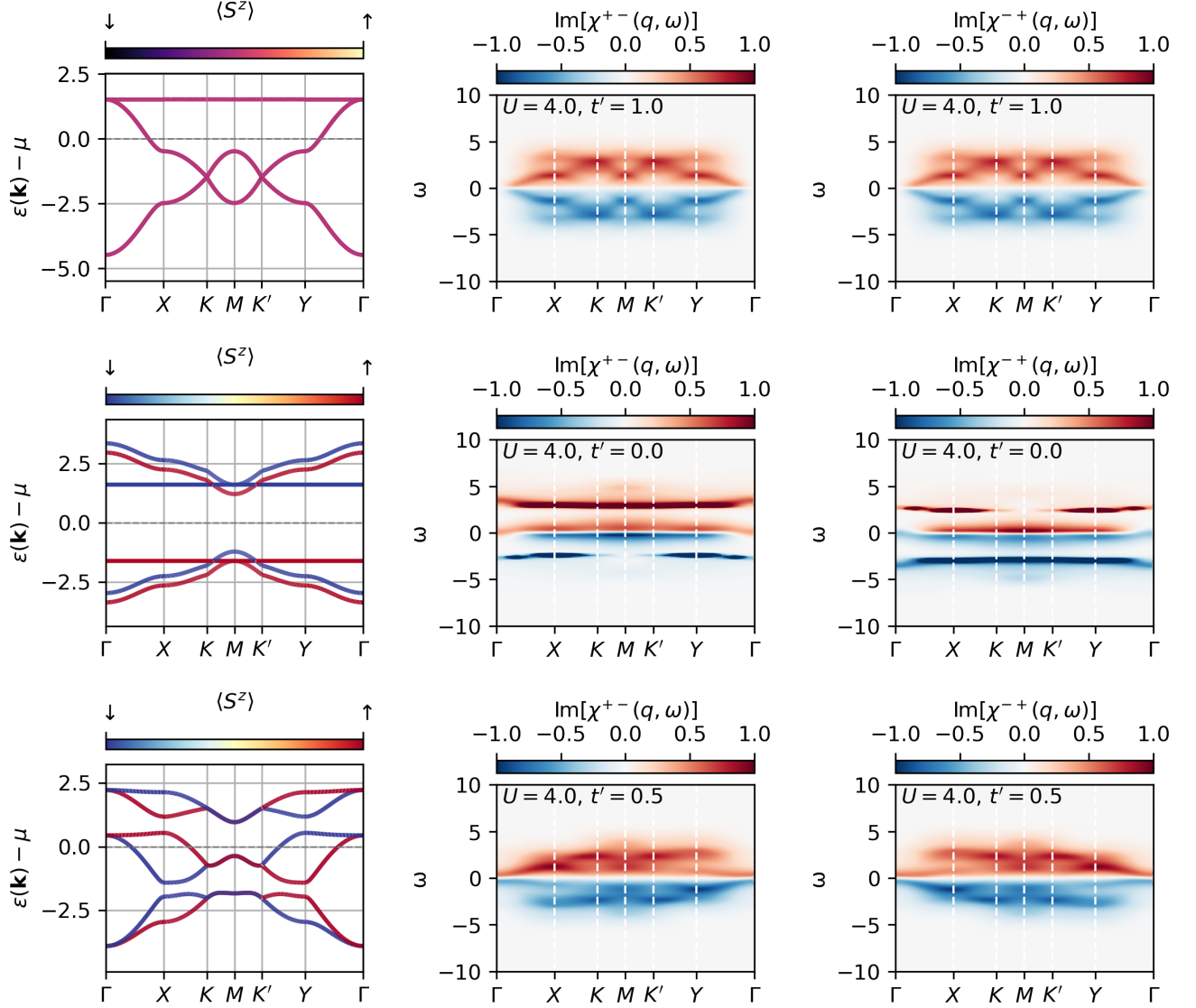


FIG. 4. Band structures and transverse spin susceptibilities  $\chi^{+-}$  and  $\chi^{-+}$  of three typical magnetic phases in the Lieb-kagome lattice with  $U = 4.0$ . Top row: The paramagnetic state with  $t' = 1.0$ , the kagome lattice limit; Middle row: The ferrimagnetic state with  $t' = 0.0$ , the Lieb lattice limit; Bottom row: The altermagnetic state with  $t' = 0.5$ .

## B. Symmetries of Transverse Susceptibility

The different magnetic phases have characteristic signatures in the electronic band structure and in the spin susceptibility. Three interesting examples are shown in Fig. 4.

The top row of Fig. 4 shows a paramagnetic solution without splitting of the electronic bands. There is no spin polarization and  $SU(2)$  symmetry is not broken. In this case, the transverse magnetic susceptibility is characterized by the symmetry

$$\Im\chi^{+-}(\omega, \mathbf{q}) = \Im\chi^{-+}(\omega, \mathbf{q}). \quad (9)$$

The susceptibility close to the  $\Gamma$  point shows the characteristic paramagnon modes with vanishing energy as

$\mathbf{q} \rightarrow 0$ .

In contrast, the middle row of Fig. 4 shows an insulating ferrimagnetic solution at  $t' = 0$  (Lieb lattice). In this case, there is an exchange splitting between  $\uparrow$  and  $\downarrow$  bands in the electronic structure, which leads to two filled majority bands and one filled minority band and therefore to a net magnetization. Both spin flavors still show the characteristic flat band of the Lieb lattice. The breaking of  $SU(2)$  symmetry leads to differences between  $\chi^{+-}$  and  $\chi^{-+}$ , but we still have the relation

$$\Im\chi^{+-}(\omega, \mathbf{q}) = -\Im\chi^{-+}(-\omega, \mathbf{q}). \quad (10)$$

For both channels, rotation symmetry within the Brillouin zone,  $\Im\chi^{+-/-+}(\omega, (q_x, q_y)) = \Im\chi^{+-/-+}(\omega, (q_y, q_x))$ , holds because of the equiva-

lence of the sites B and C. Noticeably, we can find a gapped, flat, or barely-dispersive magnon band in both majority and minority channels in the symmetry-broken ferrimagnetic phase. We refer to this as the Higgs (amplitude) magnon mode [14], which will be further discussed in the subsequent sections.

More interestingly, when the system is driven into the altermagnetic phase by applying a staggered initial field that favors altermagnetic order, the spectra display a different symmetry, as shown in the bottom row of Fig. 4 with  $U = 4.0$  and  $t' = 0.5$  as an example. For the band structure, spin splitting is visible, together with the fact that the splitting is inverted when performing a rotation in the Brillouin zone. In this case, for the magnetic susceptibility, we find that

$$\Im\chi^{+-}(\omega, (q_x, q_y)) = \Im\chi^{-+}(\omega, (q_y, q_x)), \quad (11)$$

which reflects the characteristic combination of rotational and spin-flipped symmetry of the altermagnetic state [17, 18, 31].

In textbook band theory, systems with an odd number of electrons famously have to be metallic due to the spin degeneracy of two of every band. Here, similarly, the paramagnetic and altermagnetic phases have to be metallic since we have an odd number of electrons (3 per unit cell) and both phases have bands with multiplicity two, albeit after performing a rotation in the case of the altermagnet, and thus have a spin-balanced density of states. The ferrimagnet, on the other hand, breaks the spin symmetry in the band structure and density of states, and thus allows for a spin-imbalanced insulating state. Since correlated electron systems at low temperature have a strong tendency to avoid metallicity, this explains why it is hard to stabilize altermagnetism at  $n = 3$  and easier at  $n = 2$  and  $n = 4$  [23].

### C. Ferrimagnetic Magnetization and charge redistribution

To get a deeper understanding of the phase transitions, we can study the site- and spin-dependent occupation numbers  $\langle n_{i\sigma} \rangle$ , since they play a central role in the HF approximation for the Hubbard model.

We start with the average magnetization per unit cell  $\langle S^z \rangle = \frac{1}{2} \sum_i \langle n_{i\uparrow} - n_{i\downarrow} \rangle$ . This magnetization is the order parameter of the ferrimagnetic phase and is shown as a function of  $t'$  in Fig. 5. It is also shown in color in Fig. 3. For small values of  $U$ , the magnetization drops quickly close to the ferrimagnetic-paramagnetic phase boundary. At larger values of  $U$ , there is a more gradual decrease for  $t'/t \geq 0.7$ , with the magnitude of the ferrimagnetic order parameter going continuously to zero as the antiferromagnetic phase is approached.

In addition to the magnetization per unit cell, another order parameter is the occupation of the corner site,  $n_A = \langle n_{A,\uparrow} + n_{A,\downarrow} \rangle$ , shown in Fig. 6. Since the total filling is three by construction,  $n_B = n_C = (3 - n_A)/2$ .

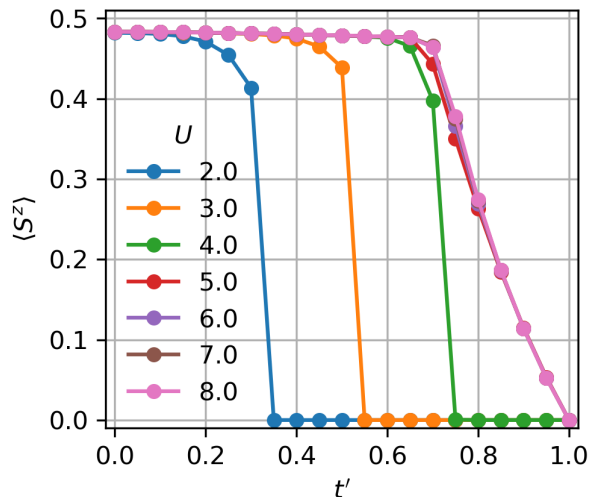


FIG. 5. Average magnetization per unit cell  $\langle S^z \rangle$  as a function of  $t'$  with different values of  $U$ .

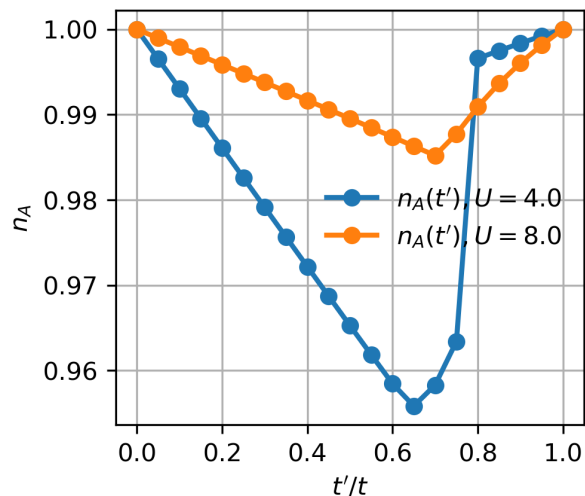


FIG. 6. Sublattice occupation at site A  $n_A$  as a function of  $t'$ . Results are shown for interaction strengths  $U = 4.0$  (blue) and  $U = 8.0$  (orange) at half-filling.

In the kagome limit at  $t'/t = 1$ , all sites are equivalent so  $n_A = 1$ . In the Lieb limit,  $t' = 0$ , particle-hole symmetry ensures that  $n_A = 1$ . In between,  $n_A$  dips slightly below 1, showing that it is beneficial to have a non-uniform charge distribution. For larger  $U$ , this effect is smaller, since the Hubbard interaction disfavors charge fluctuations.

In addition to these densities, the off-diagonal elements of the HF density matrix are also important. In particular, at large interactions, we find a solution with finite  $\langle c_{i\uparrow}^\dagger c_{j\downarrow} \rangle$ , corresponding to a spontaneously emerging spin-orbit coupling. In that case,  $S^z$  is no longer a good quantum number and we have complete breaking of the spin symmetry. To quantify the weight of  $\langle c_{i\uparrow}^\dagger c_{j\downarrow} \rangle$  within

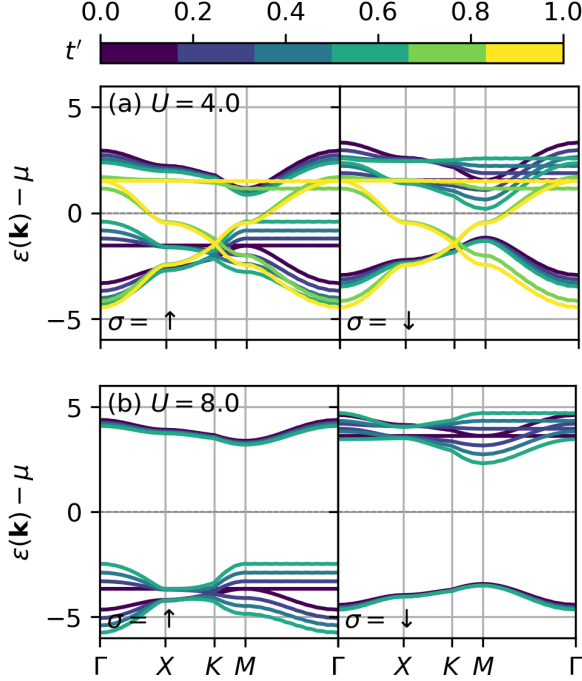


FIG. 7. Evolution of band structure with  $t'$  at (a)  $U = 4.0$ ,  $0.0 \leq t' \leq 1.0$  and (b)  $U = 8.0$ ,  $0.0 \leq t' \leq 0.6$  along the high-symmetry path.

the HF solutions, we define the off-diagonal-block ratio  $R_{\text{block}}$  as

$$R_{\text{block}} = \frac{\sum_i \sum_j |\rho_{i\uparrow, j\downarrow}| + \sum_i \sum_j |\rho_{i\downarrow, j\uparrow}|}{\sum_i \sum_j |\rho_{i\uparrow, j\uparrow}| + \sum_i \sum_j |\rho_{i\downarrow, j\downarrow}|}, \quad (12)$$

which is determined by the absolute values of the HF density matrix elements. The results of  $R_{\text{block}}$  as a function of  $t'$  with  $U = 4.0$  and  $U = 8.0$  are shown in Fig. 8. From Fig. 8, we see that the off-diagonal components of the HF density matrix are zero in the ferrimagnetic phase for both  $U = 4.0$  and  $8.0$ . However, by increasing  $t'$  at  $U = 4.0$ , the ratio  $R_{\text{block}}$  becomes finite at a point close to the AFM state and collapses to zero in the paramagnetic state, indicating a complete loss of in-plane spin-polarization in the paramagnetic phase. For  $U = 8.0$ ,  $R_{\text{block}}$  increases quickly between the ferrimagnetism-antiferromagnetism phase transition, indicating the strong in-plane polarization in this state. This will also be examined in Fig. 10.

We note that a purely Hartree approximation does not produce antiferromagnetic symmetry breaking at large  $U$ . Instead, it drives the kagome lattice toward a ferrimagnetic state with strong  $S^z$  polarization, reflecting both the odd number of bands and the inability of the Hartree term to capture geometric frustration. In contrast, the inclusion of the Fock terms, which is activated by a small transverse seed field giving the finite values of  $R_{\text{block}}$ , allows transverse spin coherences that lower the energy and stabilize the antiferromagnetic configuration

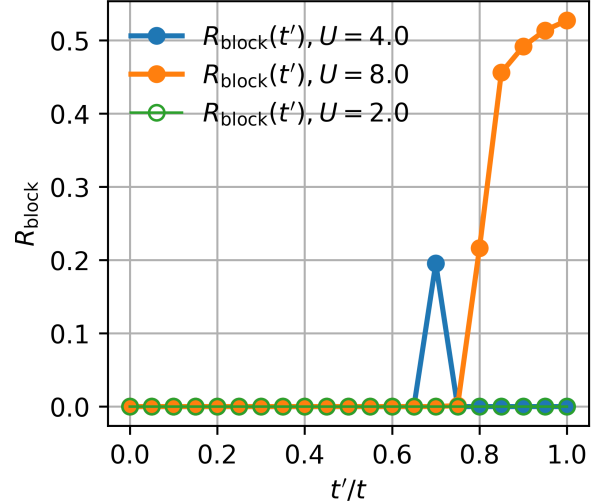


FIG. 8. Ratio of off-diagonal block to diagonal block magnitudes of the density matrix ( $R_{\text{block}}$ , defined by Eq. 12) as a function of  $t'$ .

observed in our calculations.

#### D. Band Structure Renormalization

In the HF approximation, the ferrimagnetism and charge redistribution are felt by the electrons in the form of on-site potentials and renormalization of the hopping, both spin-dependent, which lead to a renormalization of the band structure. The evolution of the band structure with  $t'$  is shown in Fig. 7, where we have restricted the plot to the regime where  $S^z$  remains a good quantum number.

At moderate interaction  $U = 4.0$ , starting from  $t' = 0$ , the spin-up and spin-down bands are separated by the orbital-dependent exchange splitting. The flat band remains flat in the presence of the interaction, but the majority flat band is below the Fermi level while the minority flat band is above the Fermi level. As  $t'$  increases, the phase transition to paramagnetism happens between  $t' = 0.6$  and  $t' = 0.8$ , as shown in Figs. 3-5. As a result, the spin-up and spin-down bands become degenerate in the paramagnetic phase.

In the strong coupling case with  $U = 8.0$ , the band gap in the ferrimagnetic case is larger because of the larger Hubbard interaction. As a result, the ferrimagnet is also more robust, and the order parameter  $\langle S^z \rangle$  remains close to its maximum value ( $\langle S^z \rangle = 1/2$ ) up to  $t'/t \lesssim 0.7$ .

For larger  $t'$ ,  $S^z$  is no longer a good quantum number and the bands have partial  $S^z$  weights as shown in Fig. 9. Simultaneously, the bands become polarized in the  $S^x$  and  $S^y$  directions, as shown in Fig. 10. In other words, the spin polarization vector of the bands rotates along the Bloch sphere, indicating the phase transition from canted ferrimagnetism, which is also observed in the quarter-

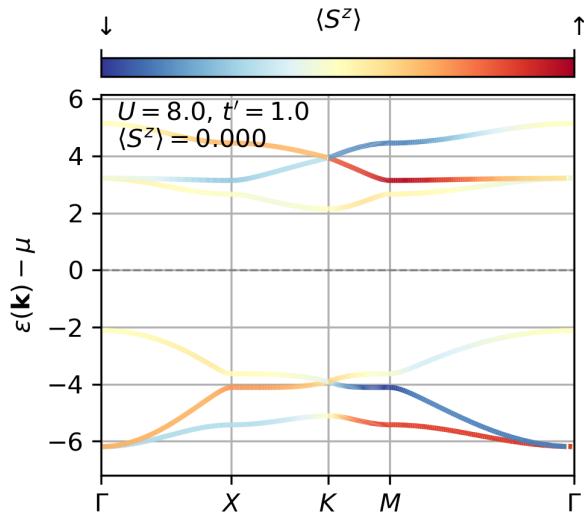


FIG. 9. Band structure colored by  $\langle S^z \rangle$  of each eigenstate with  $U = 8.0$  and  $t' = 1.0$ . The color scale represents the spin-up weight  $\sum_{i=1}^3 |\psi_i|^2$ , ranging from fully spin-down (blue) to fully spin-up (red).

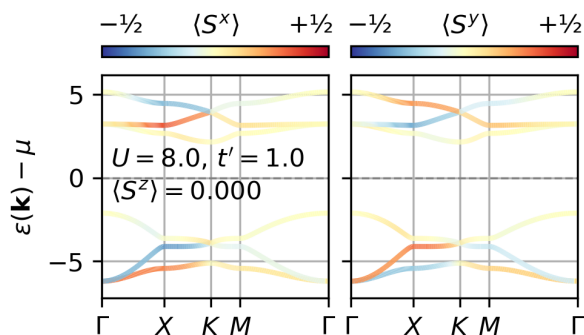


FIG. 10. Band structure colored by the transverse spin-polarization components. Left:  $\langle S^x \rangle = \sum_i \langle \psi_i | S^x | \psi_i \rangle$  ranged from fully  $-\frac{1}{2}$  (blue) to  $\frac{1}{2}$  (red). Right:  $\langle S^y \rangle = \sum_i \langle \psi_i | S^y | \psi_i \rangle$  on the same color scale. For both panels, we set  $U = 8.0$  and  $t' = 1.0$ .

filled Lieb lattice [32], to the canted antiferromagnetism. In this sense, the reduction of  $\langle S^z \rangle$  with  $t'$ , visible in Fig. 5, happens because the spin polarization of the filled bands changes continuously with  $t'$ . This also means that the concepts of minority and majority bands break down.

### E. Transverse Susceptibility Evolution

The imaginary part of the transverse bare lattice susceptibility  $\chi_0^{+-}$ , computed from the HF band structures at  $U = 4.0$ , is shown in Fig. 11. These spectra reflect the magnetic response directly computed from the renormalized single-particle bands. In the ferrimagnetic regime ( $t' \leq 0.6$ ), the dominant features are Stoner pairs exci-

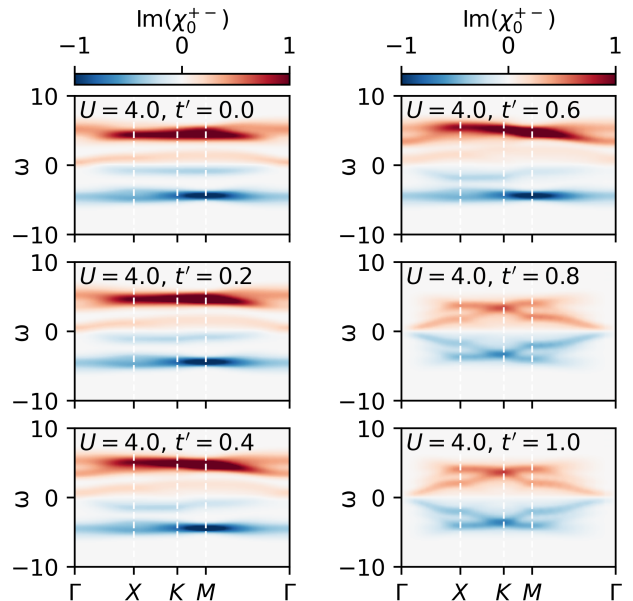


FIG. 11. Imaginary part of bare magnetic susceptibility as a function of  $t'$  with  $U = 4$ . The ferrimagnetic-paramagnetic transition takes place between  $t' = 0.6$  and  $t' = 0.8$ .

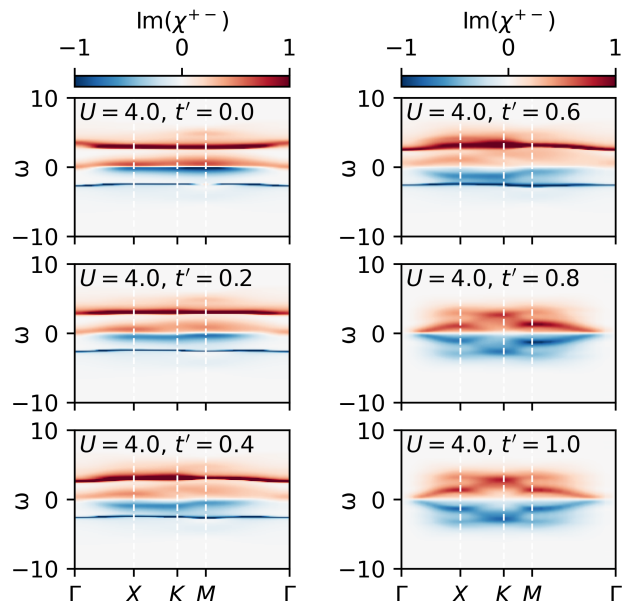


FIG. 12. Imaginary part of magnetic susceptibility computed by RPA as a function of  $t'$  with  $U = 4$ . The ferrimagnetic-paramagnetic transition takes place between  $t' = 0.6$  and  $t' = 0.8$ .

tations, which are a broad continuum of single-particle spin-flip transitions. In particular, the strong intensity around  $\omega \approx 5$  corresponds to the energy gap between the spin-up and spin-down bands in the ferrimagnetic state. We also observe weaker, but clearly resolved, minority

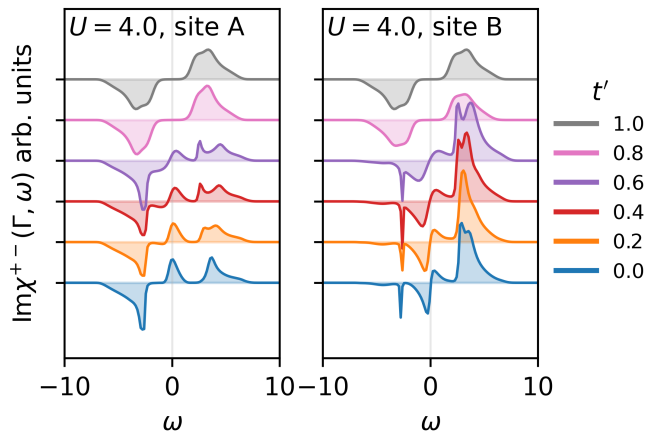


FIG. 13. Cross-section of the magnetic susceptibility  $\Im\chi^{+-}(\Gamma, \omega)$  for interaction strength  $U = 4.0$ , shown separately for site A (left) and site B (right). The comparison highlights how increasing  $t'$  shifts and reshapes the peaks of the magnetic susceptibility on the two inequivalent sublattice sites. The sharp peaks (the maximum value is shown with cutoffs in the figure, same as Figs. 15 and 19) of the Higgs modes disappear in the paramagnetic phase ( $t' = 0.8$  and  $t' = 1.0$ ).

band features consistent with the sublattice spin imbalance of the Lieb–kagome lattice. After the transition to the paramagnetic phase ( $t' \geq 0.8$ ), these ferrimagnetic features vanish, and the spectrum becomes featureless at those energies. Noting that  $\chi_0^{+-}$  only includes single-particle (bubble) processes, nevertheless, the collective magnon bands will appear at the level of the RPA.

Figure 12 shows the imaginary part of transverse susceptibility  $\chi^{+-}$  at  $U = 4.0$  computed by RPA. The transverse component involves performing a spin-flip, letting the system time-evolve, and then performing a spin-flip back, with positive and negative energies reflecting processes where the order of the  $S^+$  and  $S^-$  is interchanged,  $\chi^{+-}(\omega) = -\chi^{-+}(-\omega)$ . For small  $t'$ , the system is in the ferrimagnetic phase, and the susceptibility shows two rather flat high-energy Higgs modes which correspond to changes in the local magnetic moments. There is a Higgs mode at both positive and negative energy since it is possible to flip a majority spin on the BC sublattice or a minority spin on the A sublattice. Furthermore, there are dispersive magnon (Goldstone) modes at low energy, dispersing down to  $\omega = 0$  at  $\Gamma$ . These correspond to orienting the order parameter in another direction, which does not cost energy. Again, there are two of them, since the ferrimagnet has sites with either spin orientation. Deeper inside the Brillouin zone, broadening of the modes takes place due to the dispersion of the electronic bands, which allows for different energies for transitions with the same  $\mathbf{q}$ . Moving away from  $t' = 0$ , the flat band in the Lieb model becomes more dispersive, and this is reflected in a wider continuum in the susceptibility.

After the transition to the paramagnetic phase at

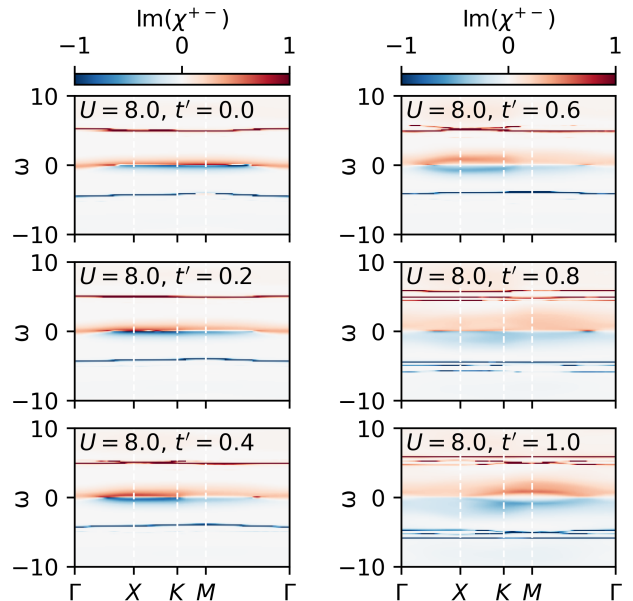


FIG. 14. Imaginary part of magnetic susceptibility computed by RPA as a function of  $t'$  with  $U = 8$ .

$t'/t \gtrsim 0.8$  for  $U = 4$ , the Higgs modes disappear, since there is no longer an order parameter to change. The Goldstone modes remain present in the form of paramagnons. Furthermore, paramagnetism leads to the equivalence of the positive and negative energy parts of the spectrum, or equivalently to  $\chi^{+-} = \chi^{-+}$ .

Figure 13 provides additional insight into the Higgs modes by looking at the site-resolved  $\Gamma$ -point susceptibility. On the minority site A, the minority Higgs mode is visible as the sharp peak at negative energy, which disappears in the paramagnetic phase ( $t' = 0.8$  and  $t' = 1$ ). The energy of the minority Higgs mode is related to the free energy landscape and is rather independent of  $t'$ . On the majority site B, for  $0 < t' < 0.8$ , some spectral weight is visible at the same negative frequency. On the other hand, most spectral weight at the B site is present at positive frequency, as expected for a spin-unbalanced system.

The transverse susceptibility  $\chi^{+-}$  for the strong coupling case  $U = 8.0$  is also plotted in Fig. 14. At  $U = 8.0$ , the static HF band splitting is larger than at  $U = 4.0$ , pushing the spin-up and -down bands farther apart. As a result, both electron-hole-pair excitation and Higgs mode appear at higher absolute energies in either the majority or minority channels. Due to the broken symmetry at larger  $U$ , the Higgs modes still exist with  $t' = 1$ , where the total average magnetization is zero, but the magnetization in the different sublattices is imbalanced in the antiferromagnetic phase.

Additionally, in Fig. 14, one observes a new, weakly dispersing mode just above the original Higgs peak with  $t' \gtrsim 0.6$ , where the phase transition of ferri- and antiferromagnetism begins to appear as shown in Fig. 5. This

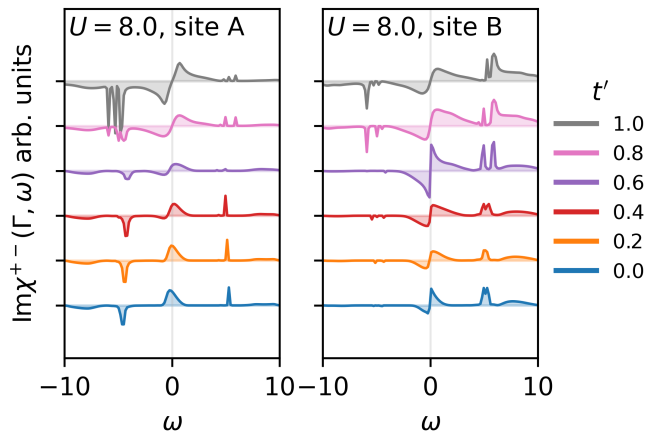


FIG. 15. Cross-section of the magnetic susceptibility  $\Im\chi^{+-}(\Gamma, \omega)$  for interaction strength  $U = 8.0$ , shown separately for site A (left) and site B (right).

additional feature likely reflects an extra Higgs mode that becomes available when the next-nearest-neighbor hopping both broadens the flat band and increases frustration when the system is close to the antiferromagnetic phase, i.e., in the upper right area of the phase diagram. By contrast, at  $U = 4.0$  (Fig. 12), the susceptibility maintains only two dominant Higgs peaks throughout the ferrimagnetic phase and disappears in the paramagnetic phase.

The site-resolved  $\Gamma$ -point susceptibility is shown in Fig. 15 with  $U = 8.0$  accordingly. Similarly, the minority site A gives the main contribution of the minority Higgs mode, whereas site B dominates the majority mode because of the unbalanced spins. The Goldstone mode broadens as  $t' \rightarrow 1$ . However, different from the case of  $U = 4.0$ , one can observe the double-peak Higgs modes for both majority and minority channels with  $t' \geq 0.6$ . We note that the Higgs modes appear as poles of the RPA susceptibility (Eq. 8), causing the exact peak heights in our spectra to depend sensitively on numerical choices (frequency grid, padding, etc.) so they should be treated with caution. The pole positions are the robust physical quantities.

#### IV. CONCLUSION

To summarize, we investigated a family of Hubbard models that interpolate between the Lieb and kagome lattices using Hartree-Fock + RPA two-particle response

calculations. The flat band in the Lieb lattice limit strongly enhances ferrimagnetic tendencies even at a small Hubbard interaction  $U$ . As the hopping parameter  $t'$  between sites  $B$  and  $C$  increases, it drives the system toward frustration-induced paramagnetic (smaller  $U$ ) and antiferromagnetic (larger  $U$ ) behavior near the kagome limit. A staggered seeding field reveals an alternating HF solution that is metastable at half-filling. In the transverse susceptibility, we find gapless dispersive Goldstone magnon modes and gapped, weakly dispersing Higgs magnon modes in the symmetry-broken region of the phase diagram. Site-resolved susceptibilities further reveal that the Higgs mode can be distinguished on different sublattices, highlighting their symmetry-breaking origin and spin-selective character.

Although the mean-field treatment overestimates the magnetic ordering in 2D, the qualitative identification of Goldstone and Higgs branches and their evolution with band geometry is robust within the same phase. These magnonic spectra, especially the coexistence of dispersive Goldstone magnons and flat Higgs modes, should be observable in inelastic probes such as neutron scattering (INS) or resonant X-ray scattering (RIXS) [33] in Lieb- or kagome-based materials with certain magnetic orders, and even other lattice systems with spontaneously-symmetry-broken features. Our findings highlight the fundamental relation between magnetic orders and magnetic excitation spectra, providing a concrete method for probing and controlling magnetic phenomena in quantum materials.

#### ACKNOWLEDGMENTS

We thank Claudio Verdozzi and Thorbjørn Skovhus for useful discussions. This work was partially supported by the Wallenberg Initiative Materials Science for Sustainability (WISE) funded by the Knut and Alice Wallenberg Foundation. EvL acknowledges support from the Swedish Research Council (Vetenskapsrådet, VR) under grant 2022-03090, from the Royal Physiographic Society in Lund and by eSENCE, a strategic research area for e-Science, grant number eSENCE@LU 9:1. HURS acknowledges financial support from the Swedish Research Council (Vetenskapsrådet, VR) grant number 2024-04652 and funding from the European Research Council (ERC) under the European Union's Horizon 2020 research and innovation programme (grant agreement No. 854843-FASTCORR).

[1] M. Qin, T. Schäfer, S. Andergassen, P. Corboz, and E. Gull, The hubbard model: A computational perspective, *Annu. Rev. Condens. Matter Phys.* **13**, 275 (2022).

[2] D. P. Arovas, E. Berg, S. A. Kivelson, and S. Raghu, The hubbard model, *Annu. Rev. Condens. Matter Phys.* **13**, 239 (2022).

- [3] J. E. Hirsch, Charge-density-wave to spin-density-wave transition in the extended hubbard model, *Phys. Rev. Lett.* **53**, 2327 (1984).
- [4] D. Geffroy, J. Kaufmann, A. Hariki, P. Gunacker, A. Hausoel, and J. Kuneš, Collective modes in excitonic magnets: Dynamical mean-field study, *Phys. Rev. Lett.* **122**, 127601 (2019).
- [5] A. Georges, L. d. Medici, and J. Mravlje, Strong correlations from hund's coupling, *Annu. Rev. Condens. Matter Phys.* **4**, 137 (2013).
- [6] H. Hafermann, E. G. C. P. van Loon, M. I. Katsnelson, A. I. Lichtenstein, and O. Parcollet, Collective charge excitations of strongly correlated electrons, vertex corrections, and gauge invariance, *Phys. Rev. B* **90**, 235105 (2014).
- [7] E. G. C. P. van Loon, H. Hafermann, A. I. Lichtenstein, A. N. Rubtsov, and M. I. Katsnelson, Plasmons in strongly correlated systems: Spectral weight transfer and renormalized dispersion, *Phys. Rev. Lett.* **113**, 246407 (2014).
- [8] A. A. Husain, E. W. Huang, M. Mitran, M. S. Rak, S. I. Ruback, X. Guo, H. Yang, C. Sow, Y. Maeno, B. Uchoa, *et al.*, Pines' demon observed as a 3d acoustic plasmon in  $\text{SrRuO}_4$ , *Nature* **621**, 66 (2023).
- [9] O. Eriksson, A. Bergman, L. Bergqvist, and J. Hellsvik, *Atomistic Spin Dynamics: Foundations and Applications* (Oxford University Press, 2017).
- [10] L. Boehnke and F. Lechermann, Competing orders in  $\text{Na}_x\text{CoO}_2$  from strong correlations on a two-particle level, *Phys. Rev. B* **85**, 115128 (2012).
- [11] J. Mušhoff, A. Kiani, and E. Pavarini, Magnetic response trends in cuprates and the  $t - t'$  hubbard model, *Phys. Rev. B* **103**, 075136 (2021).
- [12] E. G. C. P. van Loon and H. U. R. Strand, Larmor precession in strongly correlated itinerant electron systems, *Comm. Phys.* **6**, 289 (2023).
- [13] T. Skovhus and T. Olsen, Minority magnons and mode branching in monolayer  $\text{Fe}_3\text{GeTe}_2$ , *Phys. Rev. B* **110**, 165155 (2024).
- [14] D. Pekker and C. Varma, Amplitude/higgs modes in condensed matter physics, *Annu. Rev. Condens. Matter Phys.* **6**, 269 (2015).
- [15] R. Chisnell, J. Helton, D. Freedman, D. Singh, R. Bewley, D. Nocera, and Y. Lee, Topological magnon bands in a kagome lattice ferromagnet, *Phys. Rev. Lett.* **115**, 147201 (2015).
- [16] S. Riberolles, T. J. Slade, T. Han, B. Li, D. Abernathy, P. Canfield, B. Ueland, P. Orth, L. Ke, and R. McQueeney, Chiral and flat-band magnetic quasiparticles in ferromagnetic and metallic kagome layers, *Nat. Commun.* **15**, 1592 (2024).
- [17] L. Šmejkal, A. Marmodoro, K.-H. Ahn, R. González-Hernández, I. Turek, S. Mankovsky, H. Ebert, S. W. D'Souza, Šipr, Ondřej, J. Sinova, and T. Jungwirth, Chiral magnons in altermagnetic  $\text{RuO}_2$ , *Phys. Rev. Lett.* **131**, 256703 (2023).
- [18] T. A. Maier and S. Okamoto, Weak-coupling theory of neutron scattering as a probe of altermagnetism, *Phys. Rev. B* **108**, L100402 (2023).
- [19] J. Sødequist and T. Olsen, Two-dimensional altermagnets from high throughput computational screening: Symmetry requirements, chiral magnons, and spin-orbit effects, *Applied Physics Letters* **124**, 182409 (2024).
- [20] W. Jiang, M. Kang, H. Huang, H. Xu, T. Low, and F. Liu, Topological band evolution between Lieb and kagome lattices, *Phys. Rev. B* **99**, 125131 (2019).
- [21] O. Parcollet, M. Ferrero, T. Ayrál, H. Hafermann, I. Krivenko, L. Messio, and P. Seth, Triqs: A toolbox for research on interacting quantum systems, *Comput. Phys. Commun.* **196**, 398 (2015).
- [22] H. U. R. Strand, Tprf: A triqs library for two-particle response functions, <https://triqs.github.io/tprf/latest/> (2025).
- [23] N. Kaushal and M. Franz, Altermagnetism in modified Lieb lattice hubbard model, *Phys. Rev. Lett.* **135**, 156502 (2025).
- [24] E. H. Lieb, Two theorems on the Hubbard model, *Phys. Rev. Lett.* **62**, 1201 (1989).
- [25] N. D. Mermin and H. Wagner, Absence of ferromagnetism or antiferromagnetism in one- or two-dimensional isotropic heisenberg models, *Phys. Rev. Lett.* **17**, 1133 (1966).
- [26] T. Schäfer, F. Geles, D. Rost, G. Rohringer, E. Arrigoni, K. Held, N. Blümer, M. Aichhorn, and A. Toschi, Fate of the false mott-hubbard transition in two dimensions, *Phys. Rev. B* **91**, 125109 (2015).
- [27] R. Scholle, P. M. Bonetti, D. Vilardi, and W. Metzner, Comprehensive mean-field analysis of magnetic and charge orders in the two-dimensional hubbard model, *Phys. Rev. B* **108**, 035139 (2023).
- [28] R. Scholle, W. Metzner, D. Vilardi, and P. M. Bonetti, Spiral to stripe transition in the two-dimensional hubbard model, *Phys. Rev. B* **109**, 235149 (2024).
- [29] L. O. Lima, A. R. Medeiros-Silva, R. R. dos Santos, T. Paiva, and N. C. Costa, Magnetism and metal-insulator transitions in the anisotropic kagome lattice, *Phys. Rev. B* **108**, 235163 (2023).
- [30] A. Yamada, K. Seki, R. Eder, and Y. Ohta, Mott transition and ferrimagnetism in the Hubbard model on the anisotropic kagome lattice, *Phys. Rev. B* **83**, 195127 (2011).
- [31] Z. Liu, M. Ozeki, S. Asai, S. Itoh, and T. Masuda, Chiral split magnon in altermagnetic mnte, *Phys. Rev. Lett.* **133**, 156702 (2024).
- [32] A. Nikolaenko, P. M. Bonetti, A. Kale, M. Lebrat, M. Greiner, and S. Sachdev, Canted magnetism and  $z = 2$  fractionalization in metallic states of the Lieb lattice hubbard model near quarter filling, *Phys. Rev. B* **112**, 045129 (2025).
- [33] J. Mušhoff, *Susceptibility calculations for strongly correlated materials*, Ph.D. thesis, Dissertation, RWTH Aachen University, 2021 (2021).
- [34] Y. Ōno, R. Bulla, A. C. Hewson, and M. Potthoff, Critical behaviour near the metal-insulator transition of a doped mott insulator, *Eur. Phys. J. B* **22**, 283 (2001).

## Appendix A: Chemical Potential

Figure 16 shows how the reduced chemical potential  $\tilde{\mu} = \mu - \frac{1}{2}U$  in the Hubbard model that leads to half-filling evolves in the Lieb-kagome lattice by tuning  $t'$ , for  $U = 0, 4$ , and  $8$ . In the non-interacting limit,  $\tilde{\mu}$  increases smoothly with  $t'$  and reaches approximately  $0.48$  near the kagome limit. For moderate and strong interactions, the shift in chemical potential similarly approaches  $\sim 0.48$  as  $t' \rightarrow 1$ , which gives a similar result by determinant Quantum Monte Carlo (DQMC) at the temperature  $\beta = 10.0$  [29].

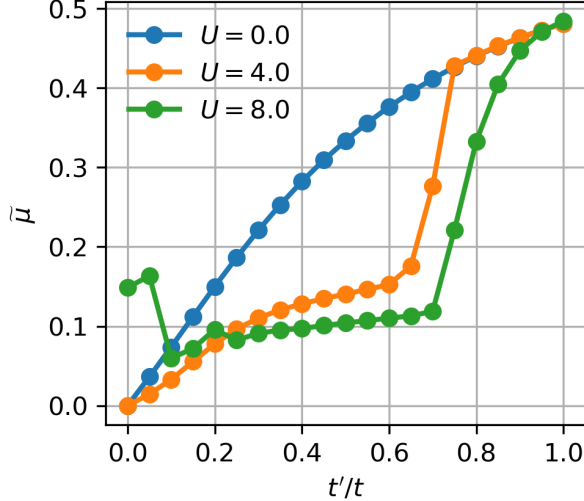


FIG. 16. The reduced chemical potential,  $\tilde{\mu} = \mu - \frac{1}{2}U$ , that leads to half-filling, plotted as a function of  $t'$  for  $U = 0.0, 4.0$ , and  $8.0$ .

For  $U = 4$  and  $U = 8$ , the dependence of  $\mu$  on  $t'$  is no longer smooth, instead showing jumps and sudden changes in slope. These changes occur when a qualitatively different mean-field solution is found. For  $U = 4$ , the jump occurs around  $t' = 0.7$  where the ferrimagnetic-paramagnetic transition takes place. For  $U = 8$ , we see several changes even within the ferrimagnetic phase. The discontinuities in the chemical potential indicate metal-insulator transitions [34].

This HF behavior contrasts with the smoother trend observed in DQMC. This difference reflects the tendency of HF to overestimate order and produce first-order jumps, whereas the exact solution does not have phase transitions in 2d, instead showing smooth cross-overs between nearly ordered phases. Still, the HF is useful to signal what kind of fluctuation is dominant.

## Appendix B: Non-interacting Model

The non-interacting system is paramagnetic and has a band structure which evolves smoothly with  $t'$ , as shown

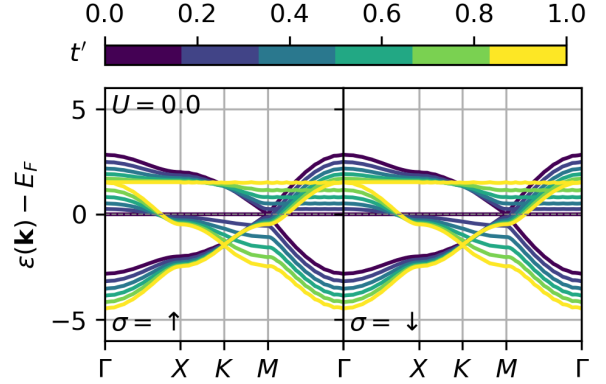


FIG. 17. Evolution of band structure as a function of  $t'$  at  $U = 0.0$

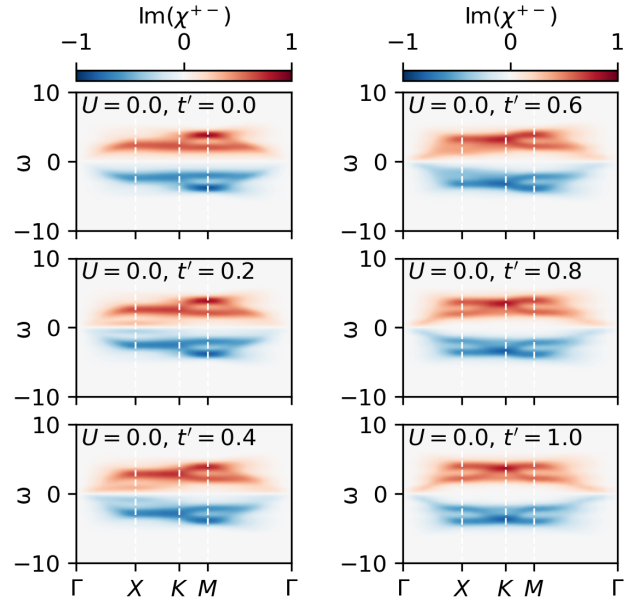


FIG. 18. Magnetic susceptibility of the non-interacting system.

in Fig. 17. Note that there is a perfectly flat band for  $t' = 0$  and  $t' = t$  only. The corresponding (bare) susceptibility is shown in Fig. 18. Due to the lack of  $SU(2)$  symmetry breaking, there is a paramagnon Goldstone mode near the  $\Gamma$  point and there is a perfect symmetry between positive and negative energies. As  $t'/t \rightarrow 1$ , the  $X - K$  and  $X - M$  sections become equivalent, while they are clearly distinct for  $t' = 0$ .

In the paramagnetic Lieb lattice, the flat band is fixed at the Fermi level and the other two bands are particle-hole symmetric, so there are relatively few different transitions and the susceptibility is dominated by a single mode for most of the Brillouin zone. The reduced symmetry for  $t' > 0$  leads to additional modes appearing in  $\chi$ . In particular, at finite  $t'$ , the previously flat band now

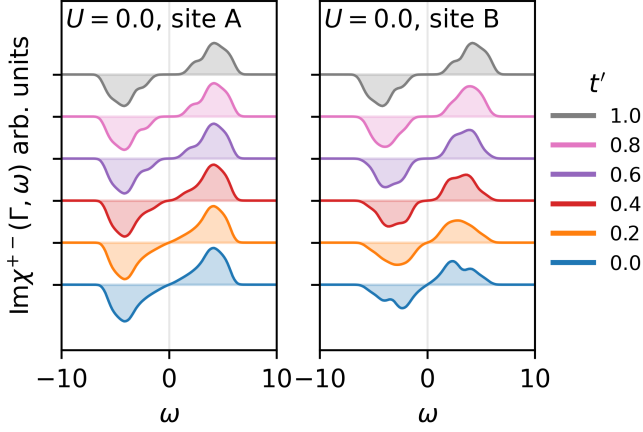


FIG. 19. Cross-section of the magnetic susceptibility at  $\Gamma$  for interaction strength  $U = 0.0$ , shown separately for site A (left) and site B (right).

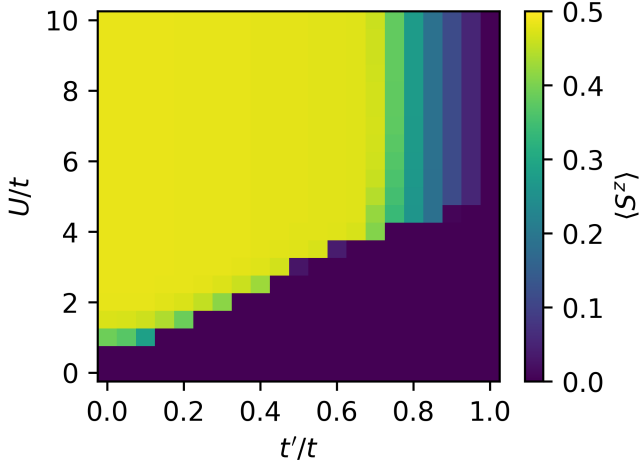


FIG. 20. Phase diagram in the HF approximation of the Lieb-kagome lattice at the temperature  $\beta = 50$ . The heatmap presents the magnetization as a function of  $U$  and  $t'$ . Similarly to the case of  $\beta = 10$ , the phase transition from ferrimagnetism (or antiferromagnetism) to paramagnetism is in the first order, and the transition from ferrimagnetism to antiferromagnetism is in the second order.

crosses the Fermi level and transitions within this almost flat give rise to low-energy features in the susceptibility.

Moving on to the site-resolved  $\Gamma$ -point susceptibility, Fig. 19 shows that A site, which is the minority site in the Lieb lattice, is relatively insensitive to  $t'$ , while the B site is more sensitive.

#### Appendix C: Temperature Effect

Figure 20 presents the same figure as Fig. 3 but with a lower temperature  $\beta = 50$  for comparison. We can ob-

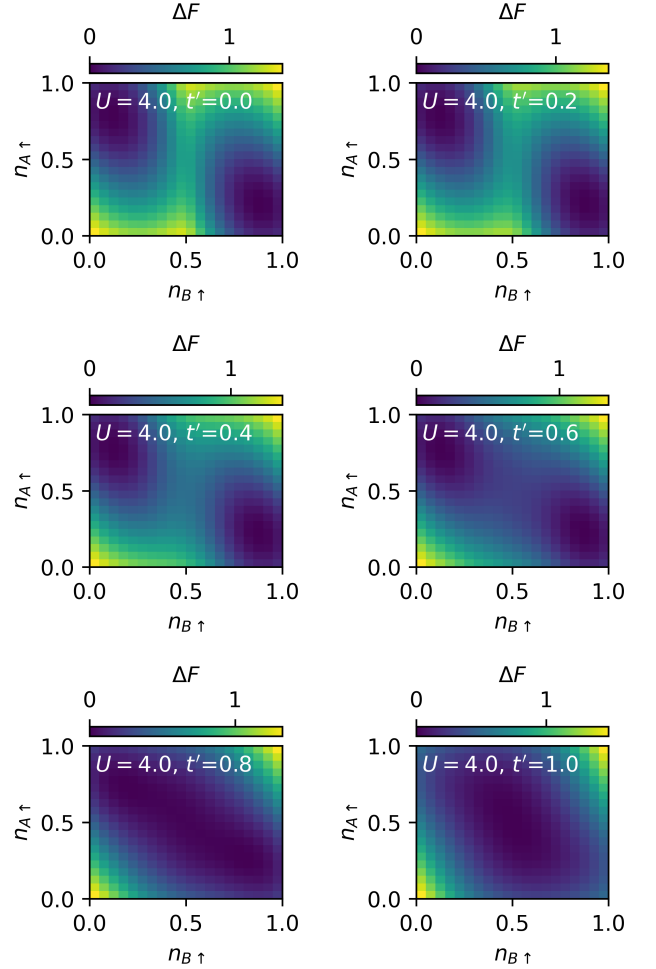


FIG. 21. Helmholtz free energy  $F$  landscapes as functions of the number of particles with spin-up at site A ( $n_{A\uparrow}$ ) and site B ( $n_{B\uparrow}$ ) with  $U = 4$ . The phase transition to paramagnetism occurs between  $t' = 0.6$  and  $t' = 0.8$ , where the lowest energy lies in the center with  $t' \geq 0.8$ , indicating no spontaneous symmetry breaking.

serve that the basic feature of the magnetic phase transition is identical for the temperature we mainly investigate in the main text, compared to the lower temperature, which demonstrates that we already approach the low-temperature limit even at  $\beta = 10$ .

#### Appendix D: Free Energy

Figures 21 and 22 show the Helmholtz free-energy difference,  $\Delta F(n_{A\uparrow}, n_{B\uparrow}) = F(n_{A\uparrow}, n_{B\uparrow}) - F_{\min}$ , mapped over the plane spanned by the spin-up occupations on sites A and B for various values of  $t'$  and interaction strengths  $U = 4$  and  $U = 8$ .

The comparison between the two interaction strengths shows how the magnetic phase and the degree of symmetry breaking evolve with increasing correlation. For

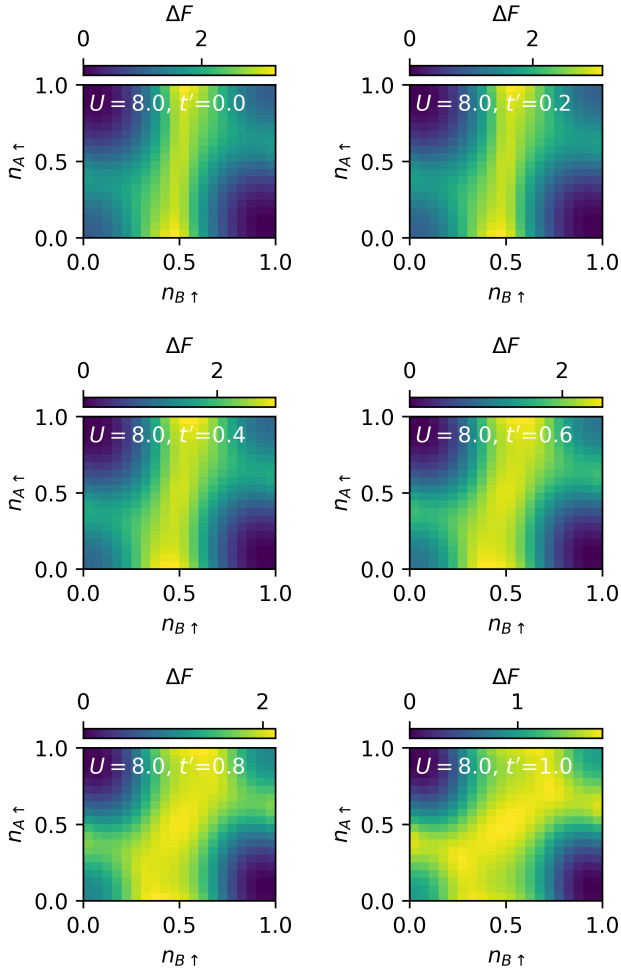


FIG. 22. Helmholtz free energy  $F$  landscapes as functions of the number of particles with spin-up at site A ( $n_{A\uparrow}$ ) and site B ( $n_{B\uparrow}$ ) with  $U = 8$ . The lowest energy at the corner indicates the symmetry-broken ferrimagnetic or antiferromagnetic states.

$U = 4$  (Fig. 21), the free-energy landscape exhibits shallow double wells that are close to the central, reflecting a weak sublattice spin imbalance and a small energy gap for amplitude (Higgs) fluctuations. As  $t' \rightarrow 1$ , the minima lie in a single symmetric valley centered at  $(n_{A\uparrow}, n_{B\uparrow}) \approx (0.5, 0.5)$ , corresponding to the paramagnetic phase without spontaneous symmetry breaking, consistent with the paramagnetic phase region shown in the phase diagram in Fig. 3. In contrast, for  $U = 8$  (Fig. 22), the free-energy minima become deeper and more separated, leading to a stable symmetry-broken magnetic ground state. The increased curvature around the minima implies a stiffer order parameter and a higher-energy Higgs mode.